Solar Phys (2009) 256: 73–85
DOI 10.1007/s11207-009-9321-1

3D Temperatures and Densities of the Solar Corona via Multi-Spacecraft EUV Tomography: Analysis of Prominence Cavities

Alberto M. Vásquez · Richard A. Frazin · Farzad Kamalabadi

Received: 18 November 2008 / Accepted: 30 January 2009 / Published online: 28 February 2009

Abstract Three-dimensional (3D) tomographic analysis of extreme ultraviolet (EUV) images is used to place empirical constraints on the corona's temperature and density structure. The input data are images taken by the EUVI instrument on STEREO A and B spacecraft for Carrington Rotation 2069 (16 April to 13 May 2008). While the reconstructions are global, we demonstrate the capabilities of this method by examining specific structures in detail. Of particular importance are the results for coronal cavities and the surrounding helmet streamers, which our method allows to be analyzed without projection effects for the first time. During this rotation, both the northern and southern hemispheres exhibited stable polar crown filaments with overlying EUV cavities. These filaments and cavities were too low-lying to be well observed in white-light coronagraphs. Furthermore, due to projection effects, these cavities were not clearly discernible above the limb in EUV images, thus tomography offers the only option to study their plasma properties quantitatively. It is shown that, when compared to the surrounding helmet material, these cavities have lower densities (about 30%, on average) and broader local differential emission measures that are shifted to higher temperatures than the surrounding streamer plasma.

STEREO Science Results at Solar Minimum.
Guest Editors: Eric R. Christian, Michael L. Kaiser, Therese A. Kucera, O.C. St. Cyr

Electronic supplementary material The online version of this article (http://dx.doi.org/10.1007/s11207-009-9321-1) contains supplementary material, which is available to authorized users.

A.M. Vásquez
Instituto de Astronomía y Física del Espacio, CONICET – University of Buenos Aires, Ciudad de Buenos Aires CC 67, Suc 28, Argentina
e-mail: albert@iafe.uba.ar

R.A. Frazin (✉)
Dept. of Atmospheric, Oceanic and Space Sciences, University of Michigan, Ann Arbor, MI 48109, USA
e-mail: rfrazin@umich.edu

F. Kamalabadi
Dept. of Electrical and Computer Engineering, University of Illinois, Urbana, IL 61801, USA
e-mail: farzadk@illinois.edu

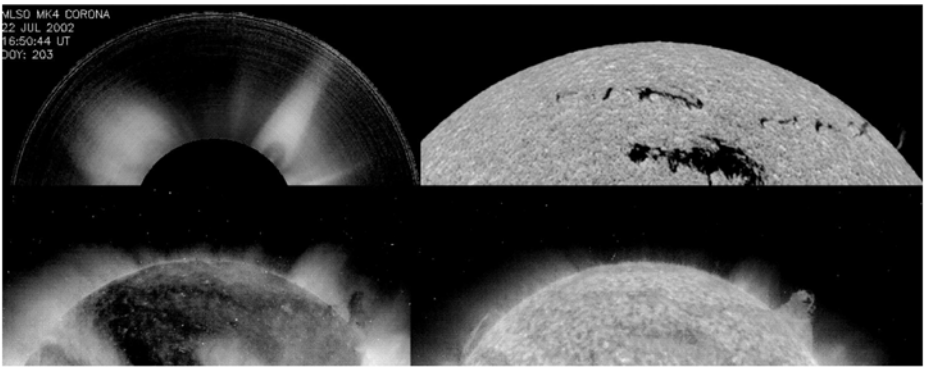

Figure 1 Images of a filament – cavity – helmet streamer in four different wavelength bands on 21 July 2002. Top left: White light (Mauna Loa Solar Observatory); top right: Hα (Big Bear Solar Observatory); bottom left: 284 Å band (NASA-SOHO/EIT); 304 Å band (NASA-SOHO/EIT). Reprinted from Gibson *et al.* (2006).

Keywords Solar corona · Filaments · Coronal cavities · Tomography · Differential emission measure · Electron density · EUV imaging · STEREO mission

1. Introduction

Filaments, also called prominences when they appear above the Sun's limb, are long ribbons of chromospheric material that reside above the rest of the chromosphere and are surrounded by coronal material (except for the lower boundary, which is part of the chromosphere). Filaments always overlie magnetic neutral lines (Babcock and Babcock, 1955), where the vertical component of the Sun's magnetic field changes sign and overlying them is a series of loop arcades that may extend up to several solar radii (R_s). These loop arcades are often seen in white-light, both in eclipse and coronagraph images, and are called helmet streamers. The inner portion of the streamer that is closest to the filament often appears much less bright than the outer loop arcades, and this region is called the cavity. Figure 1 shows observations of an example of this filament – cavity – helmet structure in multiple wavelength bands at about the same time on 21 July 2002. The upper left panel is a white-light coronagraph image showing a helmet streamer with a cavity on the right. The upper right panel is an image taken in the light of the Hα line showing the filament structure underlying the streamer and cavity. The lower left panel is an extreme ultraviolet (EUV) picture (284 Å band of EIT) exhibiting the decrease of intensity associated with the cavity overlying the filament. The image in the lower right panel, taken in the light of the EIT He II 304 Å band, shows the filament (similarly to the Hα image above it) and it is particularly clear above the limb. Besides being a ubiquitous part of the Sun's atmosphere, these filament – cavity – helmet structures have direct analogues in the observed three part structure of many coronal mass ejections (CMEs; Illing and Hundhausen, 1985) and it is known that filament eruptions are the progenitors of about 2/3 of all CMEs (St. Cyr and Webb, 1991; Gibson *et al.*, 2006). The first X-ray observations of coronal cavities were made by a series of rocket flights in the early 1970's (Vaiana, Krieger, and Timothy, 1973), and more recently observations have been made at sub-meter wavelengths (Marqué, 2004). All of this observational work shows that cavities are less dense than the surrounding helmet part of the streamer. The density depletion that forms the cavity can be understood from straightforward considerations of mass and energy balance (Pneuman, 1972;

Wolfson and Saran, 1998) as well as condensation instabilities (An, Suess, and Tandberg-Hanssen, 1985). Despite these efforts, the temperature and density structure of the filament – cavity – helmet have been difficult to quantify due to projection effects. For example, in an analysis of X-ray images of cavities with bright cores, Hudson *et al.* (1999) used several different background subtraction methods in order to estimate temperatures and densities. Fuller *et al.* (2008) treated the projection effect in white-light coronagraph data by fitting a parameterized axisymmetric taurus model to estimate the cavity density. The tomographic analysis method presented here allows us to determine the 3D temperature and density distribution, and it removes the projection effects without any assumptions about the morphology of the structures or background subtraction models. The results shown here pertaining to filament cavities represent the analysis of only a small portion of the global, 3D tomographic solutions and serve to illustrate some of the power and utility of the method.

One of the primary goals of NASA's dual-spacecraft Solar Terrestrial Relations Observatory (STEREO) mission is to determine the 3D structure of the corona (Kaiser *et al.*, 2008). The Extreme UltraViolet Imager (EUVI) on the STEREO mission returns high resolution ($1.6''$) narrow-band images centered over Fe emission lines at 171, 195, 284 Å and the He II 304 Å line (Howard *et al.*, 2008). Researchers have been using EUV and X-ray images of the Sun to derive differential emission measure (DEM) distributions, which give a measure of the amount of plasma as a function of temperature, for a number of years (Craig and Brown, 1986; Zhang, White, and Kundu, 1999; Schmelz, Kashyap, and Weber, 2007). Because the input images are two-dimensional (2D) projections of the 3D corona, the resulting DEM corresponds to an integral of all of the plasma along the line-of-sight. In this paper we remove this limitation by performing the first multi-spacecraft 3D tomography on a time series of EUV images. This procedure, in which the corona is divided into many volume elements ("voxels"), is very similar to the method for 3D density determination from white-light coronagraph images (Frazin and Janzen, 2002; Frazin and Kamalabadi, 2005). Using the information provided by multi-spacecraft views and solar rotation, the tomographic process gives the 3D emissivity in each EUV band. We then perform the local differential emission measure (LDEM) analysis on each volume element ("voxel") independently. Our technique, called differential emission measure tomography (DEMT) was described theoretically in Frazin, Kamalabadi, and Weber (2005), but it has not been applied until now. As the tomographic method is a linear inversion that assumes that the emission is from an optically thin plasma, we remove most of the optically thick regions via a statistically based data rejection technique.

Barbey *et al.* (2008) made the first steps towards tomographic determination of the 3D structure of polar plumes from EUV images, but their method requires *a priori* specification of the spatial domains that exhibit independent temporal evolution. Feng *et al.* (2007) and Aschwanden *et al.* (2008) were the first to solve the 3D geometry of coronal loops seen in EUVI images. This method is based on triangulation (sometimes called stereoscopy) and only works on loops that can be unambiguously identified in simultaneous images taken by both the "A" ("ahead") and "B" ("behind") spacecraft. Gissot *et al.* (2008) applied optical flow image processing to STEREO A and B EUVI 304 Å data and then used stereoscopy to determine the height of an erupting filament. While powerful, stereoscopic reconstruction of loops is painstaking, requires background subtraction and is not global. In contrast, our DEMT method requires no background subtraction, is global (*i.e.*, it considers the entire corona), but it does not resolve individual loops.

2. Method

Here we provide a brief introduction to the theory of DEMT. [For more detailed discussions see Frazin, Kamalabadi, and Weber (2005), and a forthcoming paper by these authors, which explains the units and other quantitative aspects.] Let $I_{k,j}$ represent the detected signal seen in the jth image pixel in the kth EUV spectral band. $I_{k,j}$ has instrument-specific units and is proportional to the intensity hitting the detector. In the optically thin limit, the intensity is related to filter band emissivity (FBE) ζ_k via a line-of-sight (LOS) integral:

$$I_{k,j} = C_k \int_{\mathrm{LOS}} \mathrm{d}l\, \zeta_k\big(\mathbf{r}_j(l)\big) + n_{k,j}, \tag{1}$$

where $n_{k,j}$ is the noise in the measurement, $\mathbf{r}_j(l)$ is a vector that traces out the LOS corresponding to the jth image pixel as a function of the scalar parameter l, and C_k is the conversion factor that goes from physical intensity units to the instrument-specific signal units. The FBE ζ_k is the plasma emissivity η times the filter transmittance $\Phi_k(\lambda)$ integrated over wavelength (λ):

$$\zeta_k(\mathbf{r}) = \int \mathrm{d}\lambda\, \Phi_k(\lambda)\eta(\lambda;\mathbf{r}). \tag{2}$$

The 3 EUVI Fe bandpasses are only sensitive to plasma with electron temperatures between about 0.5 and 3.5 MK, and, therefore, only plasma within that temperature range is seen by this analysis. Frazin and Janzen (2002) explain how to calculate $\mathbf{r}_j(l)$, taking solar rotation and spacecraft obits into account. Note that there are many pixel intensities $\{I_{k,j}\}$ because there are two spacecraft continually taking images over a number of days. Putting all of the pixel intensities in the kth spectral band into a single vector $\mathbf{I}_k$ and dividing the coronal volume into a number of separate voxels, we can discretize the integral in Equation (1) to obtain a large linear system of equations:

$$\mathbf{I}_k = \mathbf{W}_k\boldsymbol{\zeta}_k + \mathbf{n}_k, \quad 0 \le k < K, \tag{3}$$

where K is the number of filter bands ($K = 3$ in this case), $\mathbf{W}_k$ is the matrix of path lengths through the various voxels, $\boldsymbol{\zeta}_k$ is the vector of FBEs (assumed to be constant in each voxel), and the vector $\mathbf{n}_k \equiv \{n_{k,j}\,\forall j\}$ represents noise in the measured intensities. Equation (3) and the statistics of $\mathbf{n}_k$ define an independent tomographic inversion problem for each index value k. For the results presented here, the computation grid is spherical with voxels that are regularly spaced in radius, latitude and longitude (thus, the volume of the voxels increases as the radius squared) and it contains the entire volume between 1.0 and 1.26 R_s. The grid has 26 radial bins, 90 latitude bins and 180 longitude bins, so each voxel is 0.01 R_s in height (7000 km) and is $2^\circ \times 2^\circ$ [$(2.44 \times 10^4\,\mathrm{km})^2$ at the equator at 1.0 R_s].

As described in Frazin and Janzen (2002), $\mathbf{W}_k$ is a sparse matrix, which makes the inversion of Equation (3) computationally tractable. The inversion is accomplished by solving the following minimization problem:

$$\hat{\boldsymbol{\zeta}}_k = \underset{\boldsymbol{\zeta}}{\operatorname{argmin}} \left\{ \|\mathbf{I}_k - \mathbf{W}_k\boldsymbol{\zeta}\|^2 + p\|\mathbf{R}\boldsymbol{\zeta}\|^2 \right\}. \tag{4}$$

$\mathbf{R}$ is a finite difference matrix used to stabilize the inversion and force a smooth solution, and the regularization parameter $p \ge 0$ controls the amount of smoothness imposed on the solution (Demoment, 1989; Frazin and Janzen, 2002; Frazin, Kamalabadi, and Weber, 2005;

Frazin *et al.*, 2007). The value of p was chosen via a statistical procedure called cross validation (Golub, Health, and Wahba, 1979; Frazin and Janzen, 2002). The redundancy in multi-spacecraft observations (*i.e.*, viewing the Sun from the same angle at different times from different spacecraft) offers additional cross-validation opportunities not available with data sets from a single spacecraft. Note that Equation (3) does not account for the Sun's temporal variations, hence coronal dynamics in the region of one voxel can cause artifacts in neighboring voxels, including negative values of the reconstructed emissivity. The requirement for accurate reconstruction is that a given structure and its surroundings are stable in the time that they are seen by the telescopes (this is about 2 weeks in the single spacecraft case.) The issue of temporal variation in tomographic reconstruction is addressed in Frazin *et al.* (2005).

Let $\zeta_{k,i}$ be one component of the $\boldsymbol{\zeta}_k$ vector in Equation (3), *i.e.*, the value of FBE in the ith voxel. The plasma within each voxel is unlikely to all be at the same temperature, and the formalism to treat this situation is the LDEM technique introduced in Section 1. As explained above, the LDEM analysis pertains only to a single voxel, and measures the temperature distribution of the plasma that occupies it. In contrast to the LDEM, the standard DEM pertains to the entire LOS. The FBE and the LDEM $\nu_i(T)$ are related by

$$\zeta_{k,i} = \int_0^\infty \mathrm{d}T\, \nu_i(T)\psi_k(T), \tag{5}$$

where T represents the electron temperature, $\nu_i(T)$ is the LDEM in the ith voxel. Each instrument's band *DEM kernel function* $\psi_k(T)$, is the wavelength integral of its filter transmittance times the plasma emissivity in the kth band, and it is based on an optically thin plasma emission model such as CHIANTI (Young *et al.*, 2003). The LDEM $\nu_i(T)$ is proportional to N_e^2 (where N_e is the electron density) and gives a measure of the amount of plasma as a function of temperature within the voxel (Craig and Brown, 1986; Frazin, Kamalabadi, and Weber, 2005). Full details on the derivation of Equation (5), as well as the DEM kernel functions, are included in a forthcoming paper.

In DEMT, estimates of the FBE in multiple bands $\hat{\boldsymbol{\zeta}}_k$, determined from Equation (4), can give us information about the LDEM $\nu_i(T)$ through Equation (5). In principle, if enough different bands are available (*i.e.*, if K is large enough) and the kernel functions $\psi_k(T)$ show enough diversity, Equation (5) may be practically invertible (Frazin, Kamalabadi, and Weber, 2005). In the case of the data from the EUVI instrument, we use only the three Fe bands, so $K = 3$, and Equation (5) is not invertible (Schmelz, Kashyap, and Weber, 2007). A new instrument called the Atmospheric Imaging Assembly, to be launched on the Solar Dynamics Observatory, will have six Fe bands and dramatically improve the situation (Weber *et al.*, 2004; Frazin, Kamalabadi, and Weber, 2005). However, the $K = 3$ situation that presents itself does allow us to fit a Gaussian at the ith voxel, *i.e.*, assume the functional form $\nu_i(T) = \mathcal{N}(T; T_i, \sigma_{Ti}, a_i)$, where T_i, σ_{Ti} and a_i are the center, width and amplitude of the Gaussian, respectively. Aschwanden, Nightingale, and Boerner (2007) also fit Gaussians to the temperature distributions in triple filter EUV data. These three parameters are determined by minimizing the discrepancy between the tomographically determined values of $\zeta_{k,i}$ and $\int \mathrm{d}T\, \mathcal{N}(T; T_i, \sigma_{Ti}, a_i)\psi_k(T)$. Since $\nu_i(T)$ is proportional to N_e^2 (*e.g.*, Aschwanden, 2004) and the tomographically determined $\zeta_{k,i}$ are volume averages of the FBE, one obtains the root-mean-square (RMS) value of N_e by integrating the LDEM (Frazin and Kamalabadi, 2005):

$$\left\langle N_{\mathrm{e}i}^2 \right\rangle^{1/2} = \sqrt{\int_{T_\mathrm{min}}^{T_\mathrm{max}} \mathrm{d}T\, \hat{\nu}_i(T)}\,, \tag{6}$$

where $\hat{\nu}_i(T)$ is the estimate of $\nu_i(T)$ derived from the tomographic FBEs. Since $\psi_k(T)$ is dominated by Fe lines for the EUVI 171, 195 and 284 Å bands, the derived RMS N_e value is inversely proportional to the Fe abundance. In this work we assumed a constant Fe abundance of $[\mathrm{Fe}]/[\mathrm{H}] = 1.26 \times 10^{-4}$ (Feldman *et al.*, 1992), a low-FIP element abundance enhanced by a factor of about 4 with respect to typical photospheric values (Grevesse and Sauval, 1998). We also assume for the Fe ions the results given by the ionization equilibrium calculations of Arnaud and Raymond (1992). While the density variations given below could be ascribed to abundance variations, it is known from white-light observations that cavities have lower densities (see Figure 1). The streamer abundance gradients reported by Raymond *et al.* (1997) come from observations well above the maximum height of any cavities and is likely to correspond to the difference between open field at the streamer edges (from which the steady component of the slow solar wind flows) and closed field in their cores (Vásquez and Raymond, 2005). The streamer cavity is thought to be threaded by closed field as is the surrounding helmet region.

Equation (1) is only valid in the optically thin limit. The optical depth for a given LOS is defined by $\tau(\lambda) = \int_{\mathrm{LOS}} \mathrm{d}l\, \chi(\lambda, l)$, and χ is the absorption coefficient (Mihalas, 1978). The probability that a photon can travel from the far end of the LOS to the observer without being absorbed or scattered out of the LOS is $\exp(-\tau(\lambda))$, and the optically thin limit is defined as $\tau(\lambda) \ll 1$. The optical depth of the Fe lines seen in the EUVI 171, 195 and 284 Å bands is discussed in Schrijver, van den Oord, and Mewe (1994) and Schrijver and McMullen (2000). In the latter, the authors estimate that when observed in the center of the disk, about 1/2 of the photons in the 171 Å band and about 1/4 of those in the 195 Å band are scattered (the 284 Å band scattering fraction should be in between the 171 and 195 Å scattering fraction). Clearly, the largest optical depth is to be found just above and below the edge of the solar disk, where the LOS rays hit the lowest layer of the corona most obliquely. Since it is very difficult to create a precise determination of the optical depth, we used a χ^2 goodness-of-fit test (this χ has no relationship with the absorption coefficient χ), which compares the measured intensity values to the synthetic intensities determined by applying the forward model [Equation (1)] to the reconstructions, to determine an annulus of data rejection. That is, we chose to reject all pixels located between (angular) distances ρ_1 and ρ_2 from the center of the solar disk. The χ^2 test is possible since, for the work presented here, Equation (3) is overdetermined [there are about 20 times more components in the $\mathbf{I}_k$ vector than are in the $\boldsymbol{\zeta}_k$ vector]. Based on the value of the χ^2 measure, we chose to set $\rho_1 = 0.98\ R_s$ and $\rho_2 = 1.025\ R_s$ for the reconstructions in 171, 195 and 284 Å bands. In case of the reconstruction from the 304 Å data, we chose to exclude all data below $1.004\ R_s$.[1] The χ^2 analysis is presented in a forthcoming paper that covers many detailed aspects of DEMT.

3. Observations and Results

The data we analyzed consist of a 23.5 day time series of EUVI images from both the "ahead" (A) and "behind" (B) spacecraft, taken between 16 April and 9 May 2008, which is a time period corresponding to Carrington Rotation 2069. During this time period the A and B spacecraft were separated by a heliocentric angle of about 50°. This allowed 360° of view angles in 23.5 days, as opposed to 28 days as would be required for a single spacecraft.

[1] The only purpose of this the 304 Å reconstruction was to map the prominences above the limb. The reconstruction was not used for quantitative analysis due to the fact that this band is mostly sensitive to optically thick He^+ emission.

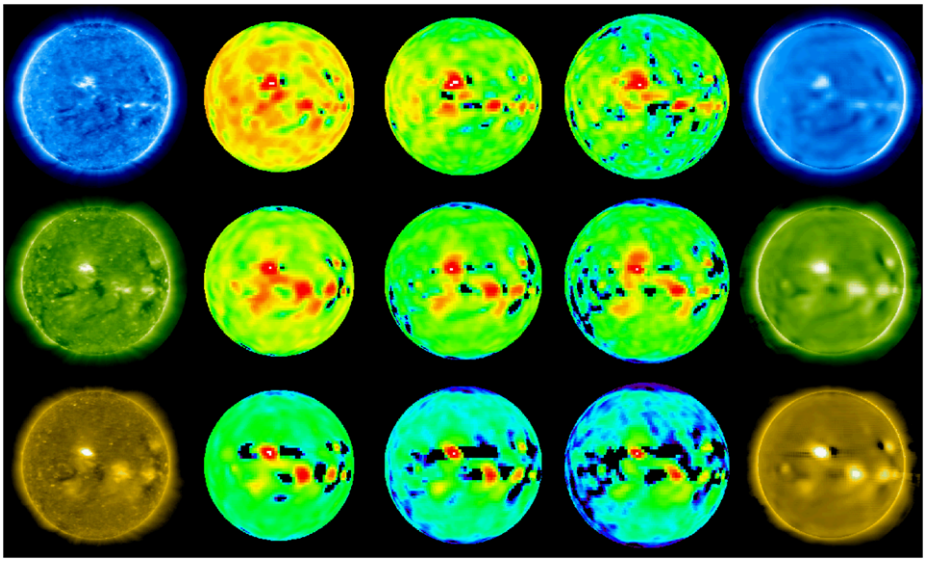

Figure 2 The first column shows the EUVI-A images in the 171, 195 and 284 Å bands taken near 08:00 UT on 28 April 2008. The second column shows projected spherical cuts of the FBE at 1.035 R_s. The projection angle of the spherical cut is chosen to be identical to that of the images in the first column. The third and fourth columns are similar, except they show spherical cuts taken at 1.085 and 1.135 R_s. The last column is a synthetic image calculated by integrating the tomographic models along the line-of-sight and thus should reasonably match the images in the first column. In all cases, we show the logarithm of the displayed quantity. For comparison purposes, the first and last columns use a common color scale for each band (row). The black streaks seen in the reconstructions near some of the active regions are artifacts caused by the Sun's temporal variability. The polar crown filaments that are the subject of this paper are clearly visible in most of the images.

We took one image every two hours from the 171, 195, 284 and 304 Å bandpasses (*i.e.*, six images in total every two hours) and, remarkably, there were no data gaps in either spacecraft or any band for the entire observation period (due to the high cadence, we used only about 5% of the available data).

Figure 2 is a graphical summary of the results of the tomography step [Equations (1) through (4)]. In the leftmost column we have EUVI-A images taken on 28 April 2008 near 08:00 UT from the 171, 195 and 284 Å bands. The middle three columns show the reconstructed FBEs on spherical shells of radius 1.035, 1.085 and 1.135 R_s, respectively. The final column shows synthetic images formed by integrating the tomographically determined FBEs along the LOS. The original images have more small-scale structure because the tomographic model does not account for dynamics at this time [although this is in progress (Frazin *et al.*, 2005)] and hence represent a type of time average of the true emissivity. The top, middle and bottom rows correspond to the 171, 195 and 284 Å bands, respectively.

The top panel of Figure 3 shows a slice of the reconstruction from the 304 Å band data at constant radius of 1.045 R_s, with boxes enclosing part of both the north and south polar crown filaments. Henceforth, these two regions in the boxes (at all heights) will be referred to as "NorthBox" and "SouthBox." The polar crown filaments show as bright, elongated structures that span roughly 100° in longitude. For example, the southern filament is easily visible between longitudes about 170° and 350° and between latitudes $-30°$ and $-50°$. The northern polar crown filament is also clearly visible as are active regions at low latitudes,

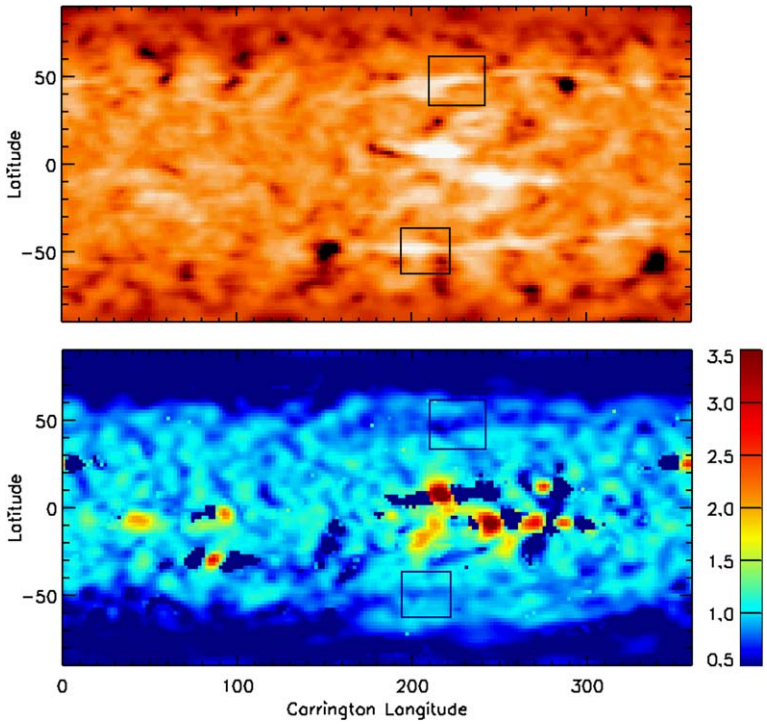

Figure 3 Top: Map of the reconstruction of the 304 Å band FBE at a height of $r = 1.045\ R_s$. While 304 Å band FBEs are not quantitatively correct due to the optical depth effects, the method is useful for mapping the filaments. Notice the north and south polar crown filaments threading the boxed regions, called "NorthBox" and "SouthBox". Bottom: Map of the RMS electron density $\langle N_e^2 \rangle^{1/2}$ at $r = 1.075\ R_s$. The density units are $10^8\,\mathrm{cm}^{-3}$, and the color scale has been thresholded for display. Cavities that exactly overlie the north and south polar crown filaments seen in the top panel are quite visible. This unambiguously shows that the filaments have overlying cavities.

which also show as bright structures on this map. We emphasize that the 304 Å band reconstruction is only useful for mapping prominences and has no straightforward quantitative interpretation due to the optically thick nature of prominence emission. The bottom panel of Figure 3 is a map at 1.075 R_s of $\langle N_e^2 \rangle^{1/2}$, as calculated from Equation (6). One can see dark streaks that are exactly spatially coincident with the polar crown filaments seen in the 304 Å emission in the top panel. This indicates that the polar crown filaments have low density cavities directly overlying them, as was assumed in the modeling effort by Fuller *et al.* (2008). Due to projection effects, the coronal cavities associated with these filaments were not clearly visible above the limb.

The top panel Figure 4 shows the LDEM curves of the longitude-averaged NorthBox at a height of 1.075 R_s and latitudes of 35°, 49°, and 61°. The 49° curve represents plasma in the heart of the cavity, while curves for 35° and 61° represent the surrounding streamer plasma. The error bars are inherited from the uncertainty in the regularization parameter p in Equation (4). The bottom panel is similar except that it refers to SouthBox. The height is the same and the latitudes are $-61°$ $-49°$, and $-37°$.

The two plots in the left column of Figure 5 refer to NorthBox and those in the right column refer to SouthBox. In each, the top plot shows the longitude averaged $\langle N_e^2 \rangle^{1/2}$ as

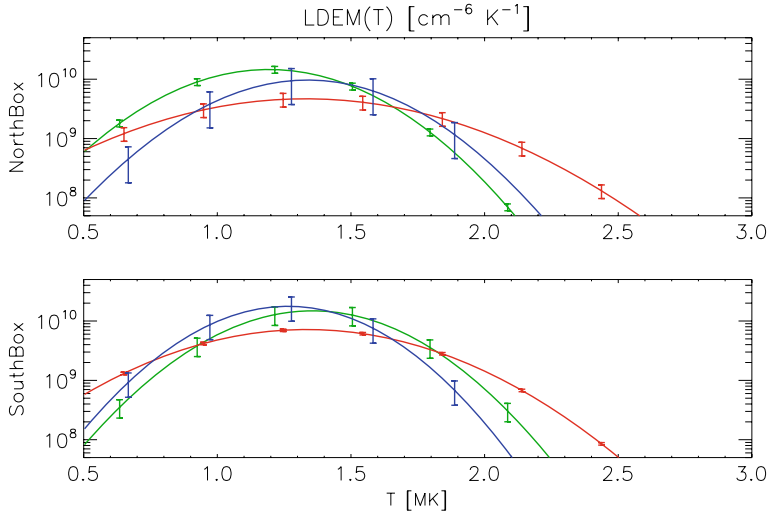

Figure 4 Top: The Gaussian fit to the LDEM in NorthBox (see Figure 3) at a height of 1.075 R_s. Each curve is determined from the 171, 195 and 284 Å FBEs averaged over longitude in NorthBox. The green and blue lines correspond to (helmet) latitudes of 35° and 61°, respectively, while the red curve corresponds to the cavity center latitude of 49°. Note that the cavity LDEM is significantly broader, containing much more plasma over 2 MK. Bottom: Similar, except for SouthBox and helmet latitudes of $-61°$ (green) and $-37°$ (blue), and cavity latitude $-49°$ (red).

a function of latitude at the height of 1.075 R_s. Similarly, the bottom plot shows the width of the Gaussian fit σ_T to the longitude averaged LDEM. One striking feature in Figure 5 is that the σ_T reaches a maximum at the latitude at which N_e reaches a minimum. To examine the relationship between these parameters in more detail, Figure 6 shows the relationship between $\langle N_e^2 \rangle^{1/2}$ and σ_T (top) and $\langle N_e^2 \rangle^{1/2}$ and T_c (bottom) for each voxel within the boxed regions at 1.075 R_s. The plots on the left are for Northbox and those on the right are for SouthBox. In both cases N_e and σ_T are negatively correlated with coefficients 0.46 (NorthBox) and 0.65 (Southbox). Similarly, $\langle N_e^2 \rangle^{1/2}$ and T_c are negatively correlated with coefficients 0.48 (NorthBox) and 0.29 (Southbox). Thus, there is a strong tendency for the analyzed regions with low density to have broader and hotter LDEMs. Since the low densities are associated with the cavity (as opposed to the surrounding helmet structure), we take this to mean that the cavity exhibits a broader and hotter temperature distribution, as is shown in Figure 4. Figure 7 shows the $\langle N_e^2 \rangle^{1/2}$ *vs.* σ_T and $\langle N_e^2 \rangle^{1/2}$ *vs.* T_c correlation coefficients (ρ) as a function of height for NorthBox (left) and SouthBox (right). We conclude that filament cavities have lower densities, and hotter, broader LDEMs than the surrounding streamer plasma associated with the 'helmet' structure.

4. Conclusions

We created 3D tomographic reconstructions of the EUVI 171, 195 and 284 Å band emissivities using data from both STEREO spacecraft taken for 23.5 days during Carrington rotation 2069 in April and May of 2008. To reduce the undesirable effects of optical depth on the tomographic reconstruction process, we ignored all the data in the images between projected radii of 0.98 and 1.025 R_s (this choice of rejection radii was determined via a statistical

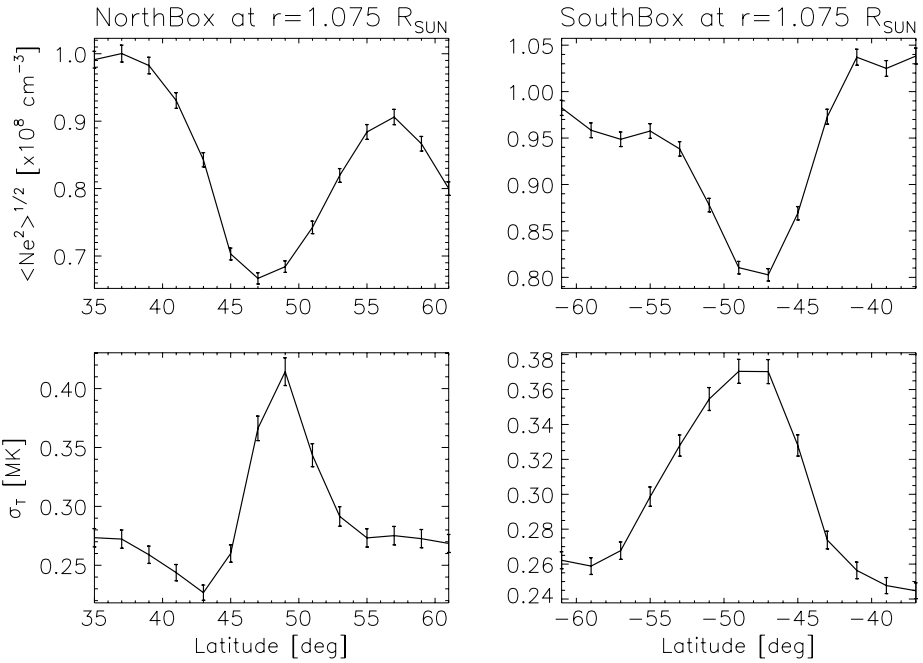

Figure 5 Properties of the Gaussian fits to LDEM of the longitude averaged FBEs in NorthBox (left) and SouthBox (right). Top: The RMS electron density $\langle N_e^2 \rangle^{1/2}$. Bottom: The width of LDEM σ_T. Notice that the LDEM width is inversely related to the density in the region of the filament cavity.

test). Using the tomographic code, we mapped the polar crown filaments in EUVI 304 Å band emission, with only above-limb data. The 304 Å map made with the tomographic code in this way is not an accurate representation of the emissivity due to optical depth effects, but it is useful for showing the locations of filaments and active regions. In all cases, the reconstruction volume extended between 1.0 and 1.26 R_s, with spherical grid spacing of $2^\circ \times 2^\circ$ in latitude and longitude and 0.01 R_s in height. Selections from these reconstructions are shown in Figures 2 and 3. We chose to analyze the portion of the north and south polar crown filament regions shown in Figure 3. These polar crown filament cavities did not reach high enough altitudes to be visible in white-light coronagraphs, and due to projection effects, these cavities were not clearly discernible above the limb in the EUV images. Thus, tomography offers the only reasonable option to study their plasma properties quantitatively.

The reconstructions show that the reduced emission of the 171, 195 and 284 Å bands exactly overlies the polar crown filaments as seen in the 304 Å maps. The LDEM was estimated from the 171, 195 and 284 Å FBEs in each voxel by fitting a Gaussian temperature distribution. In this way, the electron density $\langle N_e^2 \rangle^{1/2}$ can be computed by integrating the LDEM over temperature [Equation (6)]. The main results of the LDEM analysis are:

1. The reduced emissivity in the three Fe bands is due to a lower electron density (see the bottom panel in Figure 3, and the top panels in Figure 5), as is expected from white-light observations of filament cavities (*e.g.*, Figure 1).
2. The cavity plasma tends to have a broader LDEM distribution than the surrounding streamer (helmet) plasma. This is quantified in both Figure 5 and Figure 6, where it

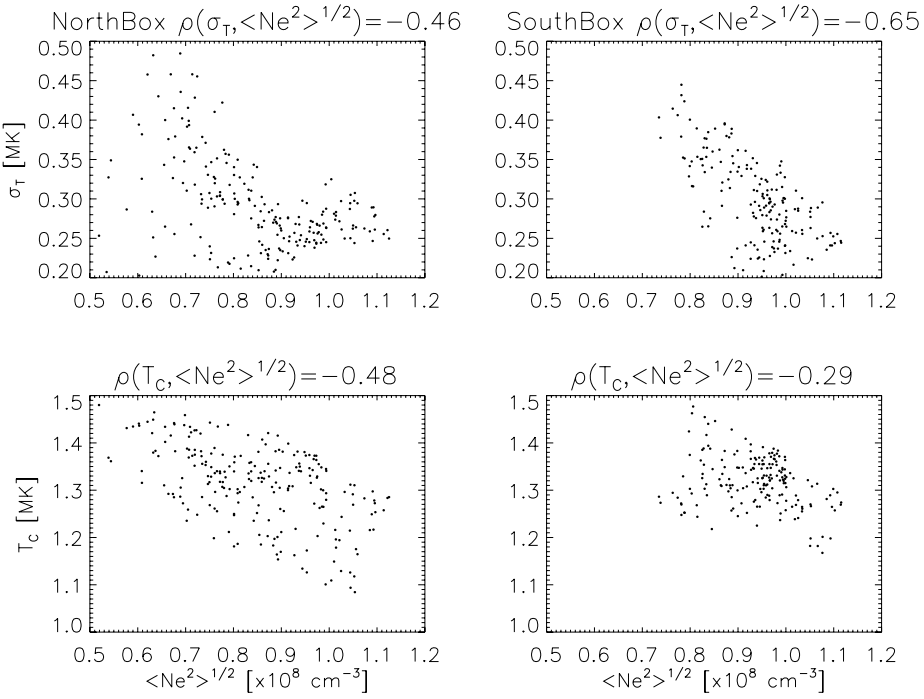

Figure 6 Scatter plots showing the relationship between LDEM quantities for each voxel at the height 1.075 R_s in NorthBox (left) and SouthBox (right). Top: $\langle N_e^2 \rangle^{1/2}$ *vs.* σ_T. Bottom: $\langle N_e^2 \rangle^{1/2}$ *vs.* T_c. The correlation coefficients ρ are shown above each plot. This demonstrates that the lower density regions tend to have broader LDEM distributions centered at higher temperatures.

is shown that N_e and the width of the LDEM σ_T are negatively correlated in the cavity – helmet region.

3. The cavity plasma tends to have a hotter LDEM than the surrounding helmet plasma. This is quantified in Figure 6, where it is shown that N_e and the center of the LDEM distribution T_c are negatively correlated.

The LDEM distributions in this work (see Figure 4) are derived under the assumption that they are Gaussian distributions. While a Gaussian is a reasonable functional form to fit to most unimodal distributions, clearly it is not adequate for more complex distributions. Furthermore, the Gaussian fits shown here are just the minimum of a cost function, and there are other admissible solutions also within the error bars. In a later paper we will use Markov chain Monte Carlo (MCMC) methods to find the class of admissible solutions (Schmelz, Kashyap, and Weber, 2007). DEM inversion ambiguities not withstanding, several features stand out:

1. At the resolution of the tomographic analysis [the voxels are 7000 km in height and roughly $(2 \times 10^4\,\mathrm{km})^2$ in basal area] both the streamer and cavity material are strongly non-isothermal, since the Gaussian curve – fit is capable of recognizing an isothermal distribution. This means that flux tubes of differing temperatures are passing through the voxels.

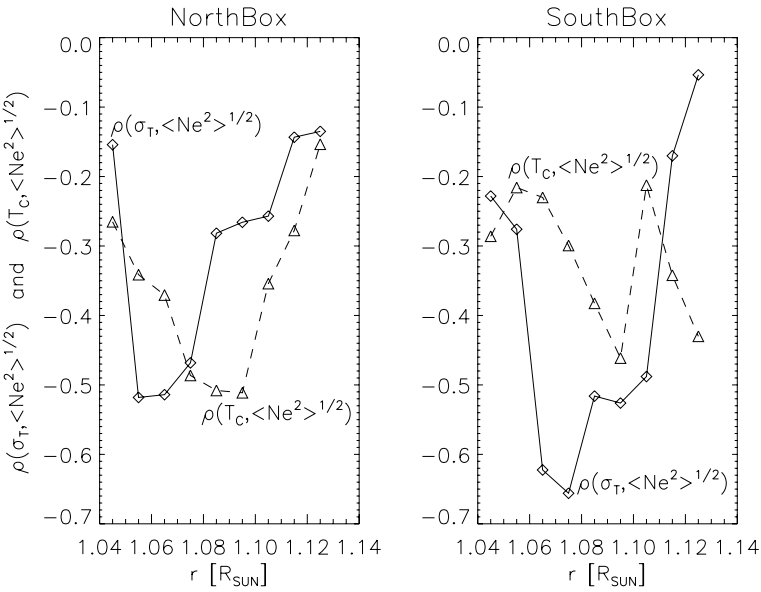

Figure 7 The correlation coefficients (see Figure 6) in NorthBox (left) and SouthBox (right), as a function of height.

2. The FBE ratios of the 171, 195 and 284 Å bands are different in the cavity than they are in the surrounding streamer material. Under the Gaussian distribution assumption, the LDEM is broader in the cavity than in the streamer, containing hotter material.
3. Unlike previous DEM analysis, which were applied to images and had to make assumptions about foreground and background structures, this 3D tomographic analysis does not suffer from line-of-sight confusion. Therefore, the conclusions drawn about the broad temperature distributions cannot be ascribed to such effects.

The main limitation of the DEMT technique applied here is the assumption that the corona is static during the data acquisition period. The method is capable of resolving structures that are stable throughout their disk transits during the studied period. The use of the twin EUVI A and B instruments, and the extension of the tomographic technique to handle simultaneous multi-spacecraft data sets, has allowed us to gather the needed data in less time than a complete solar rotation. With the $\sim 50^\circ$ angular separation of the A and B STEREO spacecraft during the studied period, we decreased the data acquisition time by about 4 days. Comparison of the first and last columns of Figure 2 shows that time-independent tomography can reproduce much of the Sun's observed structure, including the polar crown filaments studied in detail here. With the continuing separation of the STEREO spacecraft we plan to perform new global reconstructions in even less time in the near future, greatly improving capabilities of the method. These methods will be enhanced by the application of Kalman filtering to create time-dependent tomographic reconstructions (Frazin *et al.*, 2005; Butala *et al.*, 2008). Future work also will involve refining the LDEM distributions with MCMC analysis (see above), using the 6 Fe bands of the Atmospheric Imaging Assembly (AIA) on the Solar Dynamics Observatory, and analysis of other types of structures.

Acknowledgements This research was supported by NASA Heliophysics Guest Investigator award NNX08AJ09G to the University of Michigan, and the NSF SHINE and CMG programs, awards #0555561

and #0620550, respectively, to the University of Illinois. A.M.V. acknowledges the CONICET Grant PIP 6220 to IAFE for partial support. We wish to thank the anonymous referee for his/her suggestions that improved the manuscript. The STEREO/SECCHI data used here are produced by an international consortium of the Naval Research Laboratory (USA), Lockheed Martin Solar and Astrophysics Lab (USA), NASA Goddard Space Flight Center (USA), Rutherford Appleton Laboratory (UK), University of Birmingham (UK), Max-Planck-Institut für Sonnensystemforschung (Germany), Centre Spatiale de Liege (Belgium), Institut d'Optique Théorique et Appliqueé (France), Institut d'Astrophysique Spatiale (France).

References

An, C.-H., Suess, S.T., Tandberg-Hanssen, E.: 1985, *Solar Phys.* **102**, 165.
Arnaud, M., Raymond, J.C.: 1992, *Astrophys. J.* **398**, 39.
Aschwanden, M.J.: 2004, *Physics of the Solar Corona: An Introduction*, Praxis Publishing Ltd, Chichester.
Aschwanden, M.J., Nightingale, R.W., Boerner, P.: 2007, *Astrophys. J.* **656**, 577.
Aschwanden, M.J., Nitta, N.V., Wülser, J.P., Lemen, J.R.: 2008, *Astrophys. J.* **679**, 827.
Babcock, H.W., Babcock, H.D.: 1955, *Astrophys. J.* **121**, 349.
Barbey, N., Auchère, F., Rodet, T., Vial, J.-C.: 2008, *Solar Phys.* **248**, 409.
Butala, M.D., Kamalabadi, F., Frazin, R.A., Chen, Y.: 2008, *IEEE J. Sel. Top. Signal Process.* **2**, 75.
Craig, I.J.D., Brown, J.C.: 1986, *Inverse Problems in Astronomy*, Hilger, Bristol.
Demoment, G.: 1989, *IEEE Trans. Acoust. Speech Signal Process.* **7**(2), 204.
Feldman, U., Mandelbaum, P., Seely, J.L., Doschek, G.A., Gursky, H.: 1992, *Astrophys. J. Suppl. Ser.* **81**, 387.
Feng, L., Inhester, B., Solanki, S.K., Wiegelmann, T., Podipnik, B., Howard, R.A., Wülser, J.-P.: 2007, *Astrophys. J.* **671**, L205.
Frazin, R.A., Janzen, P.: 2002, *Astrophys. J.* **570**, 408.
Frazin, R.A., Kamalabadi, F.: 2005, *Solar Phys.* **228**, 21.
Frazin, R.A., Kamalabadi, F., Weber, M.A.: 2005, *Astrophys. J.* **628**, 1070.
Frazin, R.A., Butala, M.D., Kemball, A., Kamalabadi, F.: 2005, *Astrophys. J.* **635**, L197.
Frazin, R.A., Vásquez, A.M., Kamalabadi, F., Park, H.: 2007, *Astrophys. J.* **671**, L201.
Fuller, J., Gibson, S.E., de Toma, G., Fan, Y.: 2008, *Astrophys. J.* **678**, 515.
Gibson, S.E., Foster, D., Burkepile, J., de Toma, G., Stanger, A.: 2006, *Astrophys. J.* **641**, 590.
Gissot, S.F., Hochedez, J.-F., Chainais, P., Antoine, J.-P.: 2008, *Solar Phys.* **252**, 397.
Golub, G.H., Health, M., Wahba, G.: 1979, *Technometrics* **21**(2), 215.
Grevesse, N., Sauval, A.J.: 1998, *Space Sci. Rev.* **85**, 16.
Howard, R.A., Moses, J.D., Vourlidas, A., Newmark, J.S., Socker, D.G., Plunkett, S.P., *et al.*: 2008, *Space Sci. Rev.* **136**, 67.
Hudson, H.S., Acton, L.W., Harvey, K.L., McKenzie, D.E.: 1999, *Astrophys. J.* **513**, L83.
Illing, R.M.E., Hundhausen, A.J.: 1985, *J. Geophys. Res.* **90**, 275.
Kaiser, M.L., Kucera, T.A., Davila, J.M., St. Cyr, O.C., Guhathakurta, M., Christian, E.: 2008, *Space Sci. Rev.* **136**, 5.
Marqué, C.: 2004, *Astrophys. J.* **602**, 1037.
Mihalas, D.: 1978, *Stellar Atmospheres*, Freeman, New York.
Pneuman, G.W.: 1972, *Solar Phys.* **177**, 793.
Raymond, J.C., Kohl, J.L., Noci, G., Antonucci, E., Tondello, G., Huker, M.C.E., *et al.*: 1997, *Solar Phys.* **175**, 64.
Schmelz, J.T., Kashyap, V.L., Weber, M.A.: 2007, *Astrophys. J.* **660**, L157.
Schrijver, C.J., McMullen, R.A.: 2000, *Astrophys. J.* **531**, 1121.
Schrijver, C.J., van den Oord, G.H.J., Mewe, R.: 1994, *Astron. Astrophys.* **289**, L23.
St. Cyr, O.C., Webb, D.F.: 1991, *Solar Phys.* **136**, 379.
Vaiana, G.S., Krieger, A.S., Timothy, A.F.: 1973, *Solar Phys.* **32**, 81.
Vásquez, A.M., Raymond, J.C.: 2005, *Astrophys. J.* **619**, 1132.
Weber, M.A., Deluca, E.E., Golub, L., Sette, A.L.: 2004, In: Stepanov, A.V., Benevolenskaya, E.E., Kosovichev, A.G. (eds.) *Multi-Wavelength Investigations of Solar Activity*, *Proc. IAU Symp.* **223**, Cambridge University Press, Cambridge, 321.
Wolfson, R., Saran, S.: 1998, *Astrophys. J.* **499**, 496.
Young, P.R., Del Zanna, G., Landi, E., Dere, K.P., Mason, H.E., Landini, M.: 2003, *Astrophys. J. Suppl. Ser.* **144**, 135.
Zhang, J., White, S.M., Kundu, M.R.: 1999, *Astrophys. J.* **527**, 977.